Controlling the optoelectronic and anti-icing properties of two-dimensional materials by functionalization

Syari'ati, Ali

DOI:
10.33612/diss.117511370

Chapter 6

Up-scalable production of an anti-icing coating based on graphene oxide

Langmuir Schaefer deposition was chosen as upscalable production method for an anti-icing coating based on graphene oxide. Low temperature contact angle measurement confirmed a lower freezing temperature on the graphene oxide coating due to the presence of oxygen functional groups. The oxygen content of the graphene oxide was confirmed by X-Ray photoelectron and Raman spectroscopies, while the topographic characteristics of the coating layer surface were studied by means of atomic force microscopy. This work paves the way for the large-scale production of the anti-icing coatings based on two-dimensional materials.

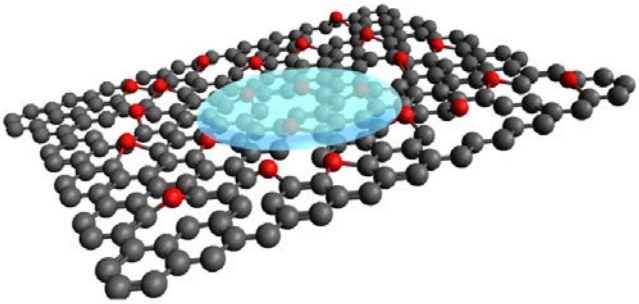

The results of this chapter will be part of a publication currently being prepared as:
Ali Syari'ati, Theodosis Giousis, Vincent Goossens, Feng Yan, Naureen Akhtar, Bodil Holst, Dimitrios Gournis, Petra Rudolf, *Up-scalable production of an anti-icing coating based on graphene oxide.*

6.1 Introduction

Ice formation is an important issue for aircrafts, drones, wind turbines, sensor and other outdoor facilities.[1–3] For these, icephobic materials have been used as coating layers to prevent or delay ice formation. The research community has focused on icing delay[4,5] and ice adhesion[6] to tackle the ice formation challenge. Icing delay refers to a material that can decrease the ice formation temperature under supercooling condition or extend the time before freezing occurs at a fixed temperature.[2] For this, hydrophobic[7,8] and biphilic[9] (which combine hydrophilic and hydrophobic regions) surfaces repel water and decrease the temperature required for freezing through different mechanisms. Biphilic surfaces influence the size and number of droplets present and thereby delay the time required for a surface to freeze even more than a purely hydrophobic surface. Ice adhesion influence how easily the ice once formed can be removed from the surface. Lubricant-based coatings suppress ice nucleation and ice adhesion by making the surface ultra-slippery.[10,11] Despite their remarkable performance as icephobic material,[12] they are not an optimal solution because they do not show the desired stability[13] in harsh environments. The work described in this chapter focuses on a icing delay coating.

Recently, Akhtar *et al.*[14] found that very defect poor, fluorinated graphene on top of a sapphire surface could decrease the freezing onset temperature from -15 °C on pure sapphire to -23 °C on the coated one. Moreover, they found that at -5 °C the fluorinated graphene coating could delay freezing by nearly 7 h, and at -15 °C by 1.5 h,[14] which is the highest freezing delay ever reported for comparable conditions.[15] Akthar *et al*. attribute this outstanding anti-icing performance of fluorinated graphene to a robust liquid layer arising from interface confinement effects that increase the viscosity of water near the surface. While these results are extremely encouraging and inspiring for future studies, they are not an answer to the practical need because the sapphire treated with this coating was no longer transparent. In fact, to achieve a defect poor graphene, they first deposited a ruthenium intermediate layer and then grew graphene on that. An additional point which is not ideal in this method is that fluorination was performed by XeF_2 plasma etching, which is rather cumbersome. On the other hand,

Geng *et al.* demonstrated the use of graphene oxide to restrict the growth of ice crystals. They highlighted the importance of the O-bearing groups on the nanosheet in controlling the ice formation suggested that these groups mimic the function of an antifreeze protein in some organisms such as fish, insects or fungi.[16–18]

In this chapter, we discuss the freezing temperature lowering produced by graphene oxide (GO) sheets, coated onto a surface to form a continuous layer by using Langmuir-Schaefer (LS) deposition. The LS method is easily upscalable to the practical dimensions of lenses and allows for arbitrary substrates to be coated. The characteristics of the as-prepared GO were studied by X-ray diffraction (XRD), Raman and X-ray photoelectron spectroscopy (XPS), while the ice formation temperature of GO-coated samples was evaluated by optically monitoring the appearance of water droplets at subzero temperatures.

6.2 Results and discussion

Graphene oxide was synthesized following a modified version of the Staudenmaier method employing concentrated sulfuric acid and nitric acid in the presence of potassium chlorate as described in ref. [19]. In detail, 5 g of graphite powder (flake size<20 μm, Aldrich) were added into a round long neck flask, containing a mixture of 200 mL of H_2SO_4 (95%-97%, Aldrich) and 100 mL HNO_3 (65%, BOOM B.V.) and while cooling in an ice water bath. 100 g $KClO_3$ (≥99%, Aldrich) were added into the mixture in small portions to avoid explosion due to the exothermic reaction, while cooling and stirring. The oxidation reaction was kept going for 18 h, then quenched by pouring the viscous mixture into a large amount of MilliQ water. The product was precipitated and washed with MilliQ water until a pH of 6.0 was reached. The resulting material was dried by spreading it onto glass plates. We used the dried GO as depicted in ***Figure 6.1*** for the experiment in this chapter.

Figure 6.1 *The photograph of GO after drying*

6.2.1 Characterizations of graphene oxide

The structural investigation was carried out using X-ray diffraction (XRD) on the freshly prepared GO collected as detailed in Chapter 2. In the diffraction pattern of GO depicted in ***Figure 6.2(a)*** the most intense peak at 10.9° corresponds to the (001) diffraction. The calculated d(001) spacing using Bragg's law of our GO is 8.0 ± 0.3 Å, which agrees with previous results of our group.[20] Taking into account that a GO layer has a thickness of 6.1 Å,[21] the interlayer separation of Δ = 8.0 – 6.1 = 2.1 Å must be due to intercalated water molecules.[22] In fact, Sasha *et al.* reported the variation of d(001) spacing in GO varied from 6.1 Å to 12 Å, depending on the amount of adsorbed water.[23] We also observed the minor peak at 21.9° that attribute to (002) diffraction of GO.

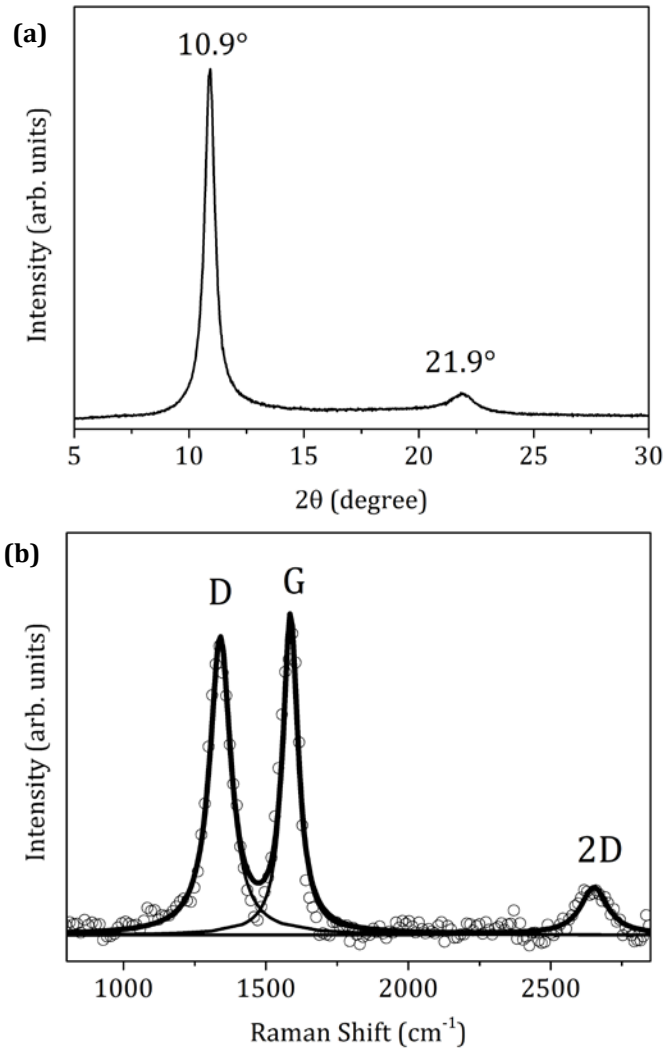

Figure 6.2 (a) *Powder XRD pattern of GO;* ***(b)*** *Raman spectrum of GO.*

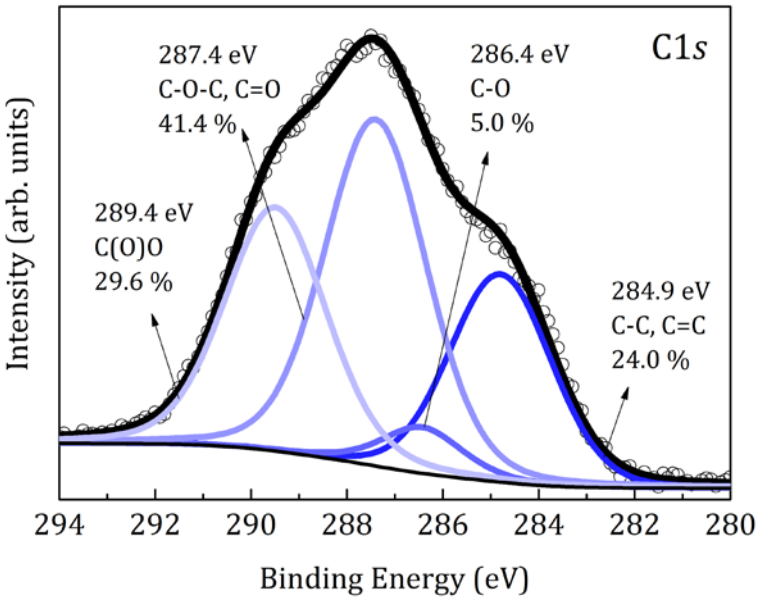

Figure 6.3 *X-ray photoelectron spectra of the C1s core level region of graphene oxide.*

We performed a Raman measurement to further confirm the presence of functional groups on the GO nanosheets. ***Figure 6.2(b)*** shows the Raman spectrum of GO (collected as described in Chapter 2), where the D, G and 2D peaks figure prominently at 1339 cm^{-1}, 1586 cm^{-1} and 2652 cm^{-1}, respectively. The G peak and the 2D peak result from the vibrations of sp^2 hybridized carbon-carbon bonds in graphene, while the D peak correlates with the presence of sp^3 hybridized carbon[24] and is associated with the presence of lattice defects and functional groups. The broad D peak accompanied by the high ratio of I(D)/I(G) of 0.9 confirms that the graphene lattice is distorted[25] due to the presence of a large amount of functional groups resulting from the oxidation process. Furthermore, the low intensity of 2D peak indicates that in GO the sp^2 network is highly disordered.[24,26]

To gain more insight into the type of functional groups and their relative abundance, we characterized the GO by XPS. As explained in Chapter 2, XPS is a surface sensitive technique that allows to determine the chemical composition of a solid surface. ***Figure 6.3*** shows the XPS spectra of C1*s* core level region, where the

component at a binding energy (BE) of 284.9 eV stems from the C-C bonds in GO and contributes 24.1% of the total carbon intensity.[20] The 5.0 % contribution of the C1*s* photoelectron peak located at 286.4 eV is ascribed to C-O bonds. The main contribution of 41.4 % of the C1*s* peak at 287.4 eV assigns to epoxy group on the basal plane of GO. Finally, the component peaked at 289.4 eV can be assigned to carboxyl groups.[23,27] The high contribution of carbon-oxygen bonds to the C1*s* spectral intensity confirms the successful oxidation of graphite, in agreement with the XRD and Raman results.

6.2.2. Graphene oxide deposition by the Langmuir-Schaefer method

We employed the Langmuir-Schaefer (LS) method to deposit the GO flakes on a SiO_2 substrate. LS is known as a well-controlled method for large scale deposition on arbitrary substrates whose dimensions are limited only by the size the LS trough. Gengler *et al.*[28] demonstrated coverage of a 3 inch Si wafer by GO deposited by the LS method. Moreover, the deposited layer has been shown to exhibit good physical properties and was not affected by harsh treatments such as a lithography process[28], which is promising for coating applications.

For film assembly a Nima Technology thermostated 612D LB trough, equipped by a Wilhelmy paper to measure the surface pressure, was filled with a subphase consisting of a stirred dispersion of 20 mg/L GO in MilliQ water. The GO-octadecylamine hybridization via covalent bonding was achieved by injecting 200 µL of octadecylamine (ODA, Sigma Aldrich, used as received) in chloroform:ethanol (9:1) solution at the surface of the subphase using a microsyringe. The ODA-GO layer floats at the air-water interface with the long chain of ODA facing towards the air and when the film is compressed at a rate of 20 cm^2/min the grafted GO flakes follow that movement. The final GO coverage on the substrate depends on the applied surface pressure at which the transfer is done. Here the GO layer was transferred onto the Si/SiO_2 substrate when the surface pressure was either 0, 20 or 30 mN/m by horizontal lowering of the substrate at a speed of 4 mm min^{-1} (downstroke) and retraction at 2 mm min^{-1} (upstroke). The transferred layer was then rinsed with MilliQ water several times and dried with a N_2 flow.

6.2.3 Characterization of graphene oxide on oxidized silicon

Figure 6.4 shows the optical microscopy images of the GO flakes deposited on SiO_2 substrate at applied surface pressures of 0 mN/m, 20 mN/m and 30 mN/m. Due to white light interference between the SiO_2 dielectric layer and the GO, one is able to observe the GO flakes on Si/SiO_2 substrate: the bare substrate is seen in purple, while the GO flakes appear in green. As expected, the low surface pressure results in low coverage of GO flakes on the substrate, as depicted in ***Figure 6.4(a)***. As shown in ***Figure 6.4(b)*** a denser packing of GO was achieved by raising the surface pressure to 20 mN/m for transfer. Transfer of a full coverage GO film can be obtained by further compressing the LS barrier to a surface pressure of 30 mN/m, as can be seen in ***Figure 6.4 (c)***. We used only full coverage samples for contact angle measurements.

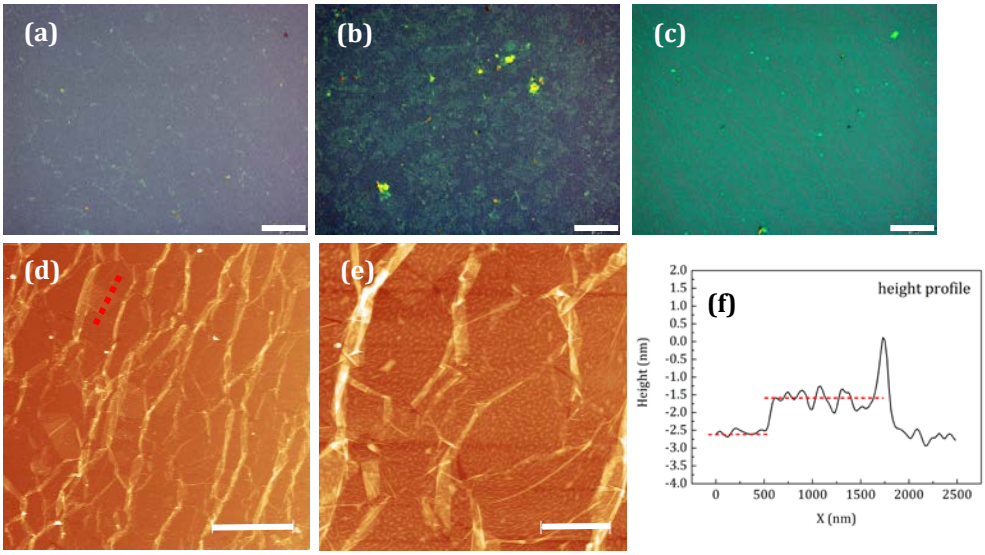

Figure 6.4 *Optical microscope images of the GO deposited on a Si/SiO_2 substrate at applied surface pressures of* ***(a)*** *0 mN/m,* ***(b)*** *20 mN/m,* ***(c)*** *30 mN/m. The white scale bar corresponds to 20 µm. AFM micrographs of a fully GO covered sample collected from areas of different size:* ***(d)*** *14 x 14 µm and* ***(e)*** *4 x 4 µm.* ***(f)*** *Topogical height profile across a second layer GO flake.*

To investigate the topography of the surface, we characterized the sample fully covered by GO using atomic force microscopy (AFM) (for the experimental details see Chapter 2). As depicted in ***Figure 6.4(d, e)*** GO forms a closely packed array with the folded/wrinkled sheets and some areas with a 2nd layer on top of the first. ***Figure 6.4(f)*** shows the topological height profile extracted from a 2nd layer GO nanosheet (red dashed line in Figure 2(d)) indicating that its thickness is 1.0±0.1 nm. The average height of the GO film was found to be 1.0 – 1.5 nm. The trace bears clear witness to the presence of the functional groups in agreement with earlier AFM studies[29] of GO, which assigned the 0.2-0.4 nm "protrusions" to the presence of isolated epoxy and hydroxyl groups; the latter can in fact attract adsorbants from the air and give rise to visible features in AFM images. As expected, the thickness value is larger than that predicted for a single GO layer (0.6 nm).[21] For this, the ODA molecules beneath the GO layer might be one of the reasons, another reason is probably due to the adsorbed water molecule as reported by Gomez *et al.*[30] and Hannes *et al.*[29] , who observed a thickness 1.1 ± 0.2 nm for a single GO layer.

6.2.4 Ice formation on bare and GO-covered oxidized silicon

We evaluated the ice formation on GO making use of a low temperature contact angle measurement set up. By cooling down the sample stage, we were able to follow the wetting properties until ice was formed. Previous studies[14,31] employed the same approach to obtain the onset temperature of freezing of a sessile droplet by observing the optical appearance during cooling process. ***Figure 6.5(a-c)*** shows the images of a water droplet on bare Si/SiO_2, while ***Figure 6.5(d-f)*** presents the images of the droplet on the same substrate covered with graphene oxide. The water droplet profile on Si/SiO_2 depicted in ***Figure 6.5(a)*** was taken at room temperature at a humidity of 50% and confirms that the surface is wettable with a contact angle of 46°±1°.

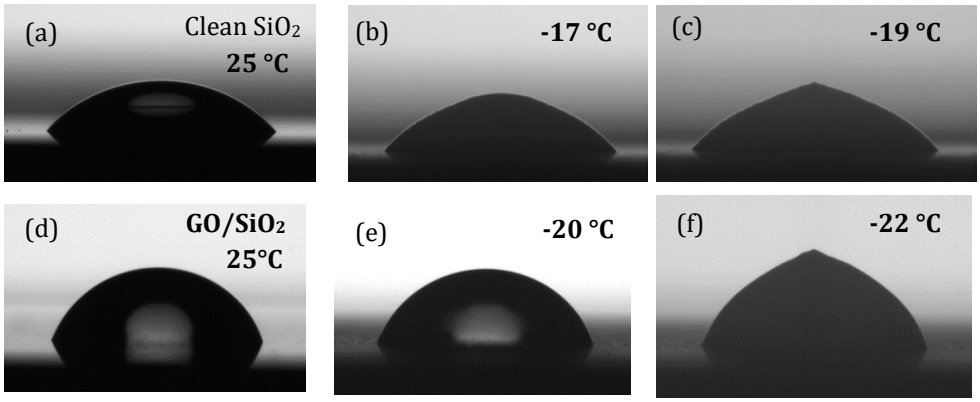

Figure 6.5. *Water droplet image taken from low temperature contact angle set up. The water droplet on clean SiO_2/Si when temperature of* ***(a)*** *25 °C,* ***(b)*** *-17 °C,* ***(c)*** *-19 °C. The water droplet on Si/SiO_2/GO when temperature of* ***(d)*** *25 °C,* ***(e)*** *-20 °C,* ***(f)*** *-22 °C.*

We then cooled down the substrate at a constant rate of 5 °C/min. As shown in ***Figure 6.5(b)***, when the temperature reached -17 °C, freezing commenced as seen from an increase of the contact angle to 53±1° accompanied by a change in the appearance of the droplet as recorded by the CCD camera. The freezing onset makes the reflection on the droplet become hazy because solid ice mixes with liquid water in the droplet. Due to the quite large distribution of the freezing onset temperature in our experiment, we observed the uncertainty of ±1 °C. After passing the freezing onset, we observed no change in droplet profile as well as the contact angle until the droplet was completely frozen at -19 °C, as shown by the image in ***Figure 6.5(c)***.

Figure 6.5(d) shows the water droplet profile on Si/SiO_2/GO as observed at room temperature (humidity 50%). The contact angle is 70°±1°, *i.e.* 24° higher than on the bare substrate. The presence of the GO layer therefore renders the surface more hydrophobic.[32] Here upon cooling the optical appearance of water droplet changed when the temperature reached -20 °C, as depicted in ***Figure 6.5(e)***. The blurry reflection of the droplet and the increase of the contact angle by 5°±1° indicate the freezing onset was reached. Complete freezing of droplet was observed when the temperature reached -22 °C. As seen in ***Figure 6.5(f)*** a little point forms on top of the droplet when the freezing process is complete. We can therefore conclude that the GO

layer decreases the freezing onset by 3 °C. We also examined the stability of the coating by repeating the icing and de-icing cycles, and found that that the freezing onset occurs always at the same temperature. However, different samples a decrease of the freezing onset by 5 °C was observed and again found to be stable on the specific sample. Unfortunately there was no time within this thesis project to study in detail how these differences are linked to the specific morphology of the coating.

The explanation of the reduced temperature of ice formation on GO is the same as put forward by Zhang *et al.*[33] when studying the icephobicity of graphene and graphene functionalized with sodium ions, chloride ions and methane molecules using molecular dynamics simulations. Unlike for three-dimensions system, microscopic theories of melting of 2D system exist and the Kosterlitz-Thouless-Halperin-Nelson-Young (KTHNY)[34] is best known one that can be used to explain the ice melting and ice formation in 2D. The KTHNY theory predicts the melting process in two steps, from the crystal to hexatic phase, then from hexatic phase to liquid.[35] The reverse process then describes ice formation. It was shown that ice formation starts with a two-dimensional (2D) wetting layer of ice molecules, on which three-dimensional (3D) ice islands nucleate and continuously grow.[33] The formation of a 2D ice layer is also supported by another report.[36] Furthermore, the ice nucleation rate is determined by the diffusion of water molecules and inversely proportional to the viscosity of the water molecules.[37] The functionalization of graphene with sodium ions, chloride ions and methane molecules results in an increase of the viscosity of water near the surface thus reducing the temperature of ice formation. Our study suggests that oxygen-containing groups on GO also push the freezing onset down based on the same mechanism.

Another study by Geng *et al.*[38] concerns the influence of GO in various concentrations in liquid water in controlling the growth and shape of ice crystals. GO prefers to adsorb on the ice crystal surface in water droplets and this gives rise to curved ice crystal surfaces.[38] This curved ice crystal surface suppresses the ice formation by lowering the ice formation temperature owing to the Gibbs-Thomson effect.[17] Gibbs-Thomson effect refers to the observation that high curvature surfaces melt at lower temperature than low curvature surfaces. In addition, molecular dynamic

simulations[38] revealed that the amount of hydrogen bonding in the water-GO mixture is less than in the ice-GO mixture, leading to a control of the ice formation at the molecular level. Geng *et al.*[38] also pointed out that such a behaviour mimics the mechanism by which the antifreeze protein (AFP) regulates the extensive network of hydrogen bonds to reduce the ice formation onset.[16]

6.3 Conclusion

In conclusion, we demonstrate that a continuous layer of GO on SiO_2/Si effectively lowers the freezing onset. The reason for the lower freezing temperature presumably resides in the increase of the viscosity of water near the surface. The upscalability of the Langmuir Schaefer method and the robustness of GO when subject to harsh treatments like lithography promises well for the technological development of GO coatings to lower ice formation in practical applications. It remains to be seen whether the freezing delay is similarly important as for F-functionalized graphene studied by Akhtar *et al.*[14] A future direction of this research could be to use LS-deposition for coating a quartz or sapphire surface with F-functionalized graphene (Fluorographene, a commercially available graphene derivative) and test its potential for lowering the freezing onset.

References

1 A. G. Kraj and E. L. Bibeau, *Renew. Energy*, 2010, **35**, 966–972.
2 Y. Shen, X. Wu, J. Tao, C. Zhu, Y. Lai and Z. Chen, *Prog. Mater. Sci.*, 2019, **103**, 509–557.
3 X. Huang, N. Tepylo, V. Pommier-budinger, M. Budinger, E. Bonaccurso, P. Villedieu and L. Bennani, *Prog. Aerosp. Sci.*, 2019, **105**, 74–97.
4 L. Cao, A. K. Jones, V. K. Sikka, J. Wu and D. Gao, *Langmuir*, 2009, **25**, 12444–12448.
5 L. Zhai, F. C. Cebeci, R. E. Cohen and M. F. Rubner, *Nano Lett.*, 2004, **4**, 1349–1353.
6 K. K. Varanasi, T. Deng, J. D. Smith, M. Hsu and N. Bhate, *Appl. Phys. Lett.*, 2010, **97**, 234102.
7 P. Roach, N. J. Shirtcliffe and M. I. Newton, *Soft Matter*, 2008, **4**, 224.
8 C. Antonini, M. Innocenti, T. Horn, M. Marengo and A. Amirfazli, *Cold Reg. Sci. Technol.*, 2011, **67**, 58–67.
9 A. S. Van Dyke, D. Collard, M. M. Derby and A. R. Betz, *Appl. Phys. Lett.*, 2015, **107**, 1–5.
10 S. A. Kulinich, S. Farhadi, K. Nose and X. W. Du, *Langmuir*, 2011, 27, 25–29.
11 M. Susoff, K. Siegmann, C. Pfaffenroth and M. Hirayama, *Appl. Surf. Sci.*, 2013, **282**, 870–879.
12 P. Kim, T. S. Wong, J. Alvarenga, M. J. Kreder, W. E. Adorno-Martinez and J. Aizenberg, *ACS Nano*, 2012, **6**, 6569–6577.
13 Z. A. Janjua, B. Turnbull, K. L. Choy, C. Pandis, J. Liu, X. Hou and K. S. Choi, *Appl. Surf. Sci.*, 2017, **407**, 555–564.
14 N. Akhtar, G. Anemone, D. Farias and B. Holst, *Carbon N. Y.*, 2019, **141**, 451–456.
15 P. Guo, M. Wen, L. Wang and Y. Zheng, *Nanoscale*, 2014, **6**, 3917–3920.
16 Y. C. Liou, A. Tocilj, P. L. Davies and Z. Jia, *Nature*, 2000, **406**, 322–324.
17 C. A. Knight, *Nature*, 2000, 406, 249–251.
18 F. Shi, J. Niu, J. Liu, F. Liu, Z. Wang, X. Q. Feng and X. Zhang, *Adv. Mater.*, 2007, **19**, 2257–2261.
19 K. Spyrou, G. Potsi, E. K. Diamanti, X. Ke, E. Serestatidou, I. I. Verginadis, A. P. Velalopoulou, A. M. Evangelou, Y. Deligiannakis, G. Van Tendeloo, D. Gournis and P. Rudolf, *Adv. Funct. Mater.*, 2014, **24**, 5841–5850.
20 K. Spyrou, M. Calvaresi, E. K. Diamanti, T. Tsoufis, D. Gournis, P. Rudolf and F. Zerbetto, *Adv. Funct. Mater.*, 2015, **25**, 263–269.
21 I. Dékány, R. Krüger-Grasser and A. Weiss, *Colloid Polym. Sci.*, 1998, **276**, 570–576.
22 S. Zheng, Q. Tu, J. J. Urban, S. Li and B. Mi, *ACS Nano*, 2017, **11**, 6440–6450.
23 S. Stankovich, D. a. Dikin, R. D. Piner, K. a. Kohlhaas, A. Kleinhammes, Y. Jia, Y. Wu, S. T. Nguyen and R. S. Ruoff, *Carbon N. Y.*, 2007, **45**, 1558–1565.
24 A. C. Ferrari and D. M. Basko, *Nat. Nanotechnol.*, 2013, **8**, 235–246.
25 A. C. Ferrari and J. Robertson, *Phys. Rev. B*, 2000, **61**, 14095–14107.
26 A. C. Ferrari, *Solid State Commun.*, 2007, **143**, 47–57.
27 Y. V Butenko, S. Krishnamurthy, A. K. Chakraborty, V. L. Kuznetsov, V. R. Dhanak, M. R. C. Hunt and L. Šiller, *Phys. Rev. B*, 2005, **71**, 075420.
28 R. Y. N. Gengler, A. Veligura, A. Enotiadis, E. K. Diamanti, D. Gournis, C. Józsa, B. J. van Wees and P. Rudolf, *Small*, 2010, **6**, 35–39.
29 H. C. Schniepp, J. L. Li, M. J. McAllister, H. Sai, M. Herrera-Alonson, D. H. Adamson, R. K. Prud'homme, R. Car, D. A. Seville and I. A. Aksay, *J. Phys. Chem. B*, 2006, **110**, 8535–8539.
30 C. Gómez-Navarro, R. T. Weitz, A. M. Bittner, M. Scolari, A. Mews, M. Burghard and K. Kern, *Nano Lett.*, 2007, **7**, 3499–3503.
31 S. Jung, M. Dorrestijn, D. Raps, A. Das, C. M. Megaridis and D. Poulikakos, *Langmuir*, 2011, **27**, 3059–3066.
32 R. Rasuli, Z. Mokarian, R. Karimi, H. Shabanzadeh and Y. Abedini, *Thin Solid Films*, 2015, **589**, 364–368.
33 X.-X. Zhang and M. Chen, *J. Nanomater.*, 2016, **2016**, 1–8.

34 A. J. Page and R. P. Sear, *Phys. Rev. E*, 2009, **80**, 031605.
35 J. M. Kosterlitz and D. J. Thouless, *J. Phys. C Solid State Phys.*, 1972, **5**, L124–L126.
36 L. H. Seeley and G. T. Seidler, *Phys. Rev. Lett.*, 2001, **87**, 55702-1-55702–4.
37 K. Li, S. Xu, J. Chen, Q. Zhang, Y. Zhang, D. Cui, X. Zhou, J. Wang and Y. Song, *Appl. Phys. Lett.*, 2014, **104**, 101605.
38 H. Geng, X. Liu, G. Shi, G. Bai, J. Ma, J. Chen, Z. Wu, Y. Song, H. Fang and J. Wang, *Angew. Chemie - Int. Ed.*, 2017, **56**, 997–1001.